6 | https://doi.org/10.3311/PPme.22045
Creative Commons Attribution

Periodica Polytechnica Mechanical Engineering, 68(1), pp. 6–17, 2024

Lattice Boltzmann Simulation of Incompressible Fluid Flow in Two-sided Converging and Diverging Lid-driven Square Cavity

Mahendra Yadav[1], Rajendra Singh Yadav[1*], Oluwole Daniel Makinde[2], Pankaj Mathur[3]

[1] Department of Mathematics, University of Rajasthan, JLN Marg, 302004 Jaipur, Rajasthan, India
[2] Faculty of Military Science, Stellenbosch University, 7602 Matieland, P.O.B. X1, South Africa
[3] Department of Mathematics, Government College, Baheer Road, 304001 Tonk, Rajasthan, India
[*] Corresponding author, e-mail: rajendrauor@gmail.com

Received: 12 February 2023, Accepted: 18 December 2023, Published online: 01 February 2024

Abstract

The present study focuses on the predictions of flow behavior, streamlines and some other factors of a two adjacent-sided converging and diverging lid-driven square cavity filled with fluid. In the diverging case, the top wall of the cavity is considered to be in motion from left to right, and the left wall is considered to be in motion from top to bottom simultaneously with identical speeds. It is found that for a low Reynolds number, the flow behavior seems to be symmetric with respect to one of the diagonals of the cavity, and at a critical Reynolds number 1121, the symmetry of the flow behavior blows up, and an asymmetric form is obtained due to the increased inertia and turbulence effects. Any increment in the Reynolds number above the critical Reynolds number develops this asymmetry gradually more and more. In the second phenomenon, the converging phenomenon, the top wall of the cavity is assumed to be in motion from left to right, and the right wall is assumed to be in motion from bottom to top simultaneously with identical speeds so that they converge at the corner of the cavity. This case gives rise to two critical Reynolds numbers Re = 969 and Re = 2053 and the flow behavior for both asymmetric states was found to be opposite. Furthermore, the rate of convergence of the present methodology, lattice Boltzmann methodology, for various Reynolds numbers is found to be very high except for the critical and their nearby Reynolds numbers.

Keywords

Chapman-Enskog theory, diverging driven cavity, converging driven cavity, skin friction coefficient, kinetic energy density function

1 Introduction

The study of numerical simulations of Navier-Stokes equations has been a versatile topic of interest among researchers for the past century. Many numerical approaches have succeeded so far in simulating Navier-Stokes equations under certain limiting conditions. The analytic solutions of Navier-Stokes equations are still the most significant undiscovered problem in the history of fluid dynamics. The present work uses the application of the Navier-Stokes equation in the form of a vorticity-streamline function to simulate and validate two adjacent-sided lid-driven square cavities using the lattice Boltzmann approach.

The lid-driven square cavity problem is an all-time preferred problem for testing and validating new numerical methodologies. Many studies in the field of the one-sided lid-driven square cavity and two-sided (parallel and anti-parallel) lid-driven square cavity have been carried out experimentally and numerically. Aidun et al. [1] interpreted the global stability of single-sided lid-driven cavity flow. Later, Shankar and Deshpande [2] compared the experimental and computational results for one-sided lid-driven cavity flow. In which they computed corner eddies, longitudinal vortices, non-uniqueness, transition, and turbulence of the flow. Wahba [3] discussed the behavior of two-sided and four-sided lid-driven cavity flow for low Reynolds numbers using the finite difference method, and concluded that the choice of the sweeping direction line determines the solutions' state. Mendu and Das [4] simulated lid-driven cavity flow with a periodically oscillating lid. Biswas and Kalita [5] gained some physical insights of the topology of corner vortices in 2D vis a 3D vis driven cavity. Dalai and Laha [6] interpreted the conservative solutions of Navier-Stokes equations (NSEs) in the stream function-vorticity form.

Cite this article as: Yadav, M., Singh Yadav, R., Makinde, O. D., Mathur, P. "Lattice Boltzmann Simulation of Incompressible Fluid Flow in Two-sided Converging and Diverging Lid-driven Square Cavity", Periodica Polytechnica Mechanical Engineering, 68(1), pp. 6–17, 2024.
https://doi.org/10.3311/PPme.22045

Sikdar et al. [7] discussed the inertia effect at different moving lengths of the top lid. However, all these studies were based on the traditional numerical methods.

Abedini et al. [8] addressed a new computational technique for NSEs with time-fractional order in the Caputo sense. Álvarez Hostos et al. [9] proposed a coupled improved element free Galerkin reduced integration pentaly method (IEFG-RIPM) to simulate steady state lid driven cavity phenomenon. Azzouz and Houat [10] numerically demonstrated the fluid flow inside a three-sided lid driven square cavity. They used the finite volume method on a fine mesh resolution with pressure-velocity coupling. Patel et al. [11] performed a different kind of study using the same finite volume method on a four-sided lid driven square cavity. Turkyilmazoglu [12] divided the upper wall into two parts of equal lengths. The right part of the wall is left for freely to move with constant velocity whereas left part of the wall is attached with an adjacent wall to maintain its velocity. Zhang et al. [13] used the lattice Boltzmann method (LBM) to study the fluid flow structures in multi sided lid driven sqaure cavities for eight different cases. The results found to be very much accurate comparing to the exiting literatures and that proves the robustness and accurateness of the LBM technique.

Therefore, the quality of being a highly accurate method proves the importance of the lattice Boltzmann method over traditional computational methods in various literature. Due to its simplicity and easy implementation, the lattice Boltzmann method (LBM) has become a well-liked and widely used computational fluid dynamics (CFD) simulation tool. This method is based on the macroscopic model and uses the kinetic theory of gases to develop mesoscopic equations for particle distribution function [14–16], which makes this method to be macroscopically accurate and hence, this method directly simulates the behavior of fluid flow instead of solving macroscopic equations. Initially, this method originated from the theory of lattice gas cellular automata (LGCA) by Hardy et al. [17, 18] for hydrodynamic models (also known as HPP models). After a decade, Frisch et al. [19] derived a hexagonal grid model (FHP model), which uses six or seven velocities (one is at rest) to reach neighboring nodes, to acquire the correct Navier-Stokes equations. Chen et al. [20] obtained the correct Navier-Stokes equations through the pressure corrected lattice Boltzmann equation. He and Luo [21, 22] obtained lattice Boltzmann equation explicitly by the discretization of continuous Boltzmann equation in both time and phase space, and that is how this methodology was developed. This LB method has been successfully demonstrated for the many applications of fluid flows so far, such as complex and turbulent flows, Rayleigh-Taylor instability between two fluids, multiphase flows, porous media flow, viscoelastic fluid flows, magneto hydrodynamics, etc.

The Lattice Boltzmann Method is a two-step method: streaming and collision. In streaming, particles propagate from one lattice site to another, and then collision takes place. Many approximations for the collision process have developed in the theory of the Lattice Boltzmann method [14]. The simplest and most used approximation for the collision operator is the LBM-BGK [23] approximation, which is based on a single relaxation time (SRT) scheme.

This article chooses two-adjacent-sided diverging and converging lid-driven square cavities to study fluid behavior at various Reynolds numbers and their properties. Lattice Boltzmann method (LBM) with a single relaxation time scheme is adapted for simulation with a two-dimensional nine velocities (D2Q9) square model, and the bounce-back boundary conditions are introduced for the moving walls as well as for the stationary walls.

2 Problem statement

The schematic diagram of the two adjacent-sided diverging lid-driven square cavity and two adjacent-sided converging lid-driven square cavity with appropriate boundary conditions are shown in Figs. 1 and 2. In the diverging case (Fig. 1), the walls diverge from point A and in the converging case (Fig. 2), the walls are considered to be converging at point B. The other non-moving two walls are kept stationary in both cases. Initially, at $t = 0$, the velocity components (u, v) are chosen to be zero at all grid points except on the boundaries for the cavity. Moreover,

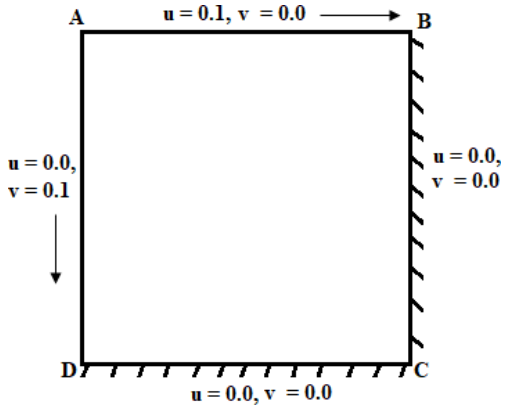

Fig. 1 Two adjacent-sided diverging lid-driven square cavity

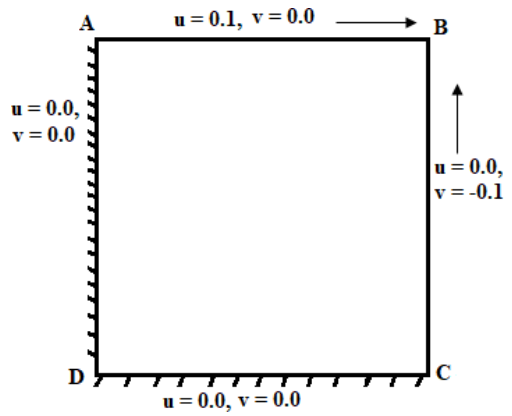

Fig. 2 Two adjacent-sided converging lid-driven square cavity

a uniform incompressible fluid flow is considered for both phenomena, which is governed by the following Navier-Stokes (N-S) equations (Eqs. (1)–(3)):

$$\frac{\partial u}{\partial x}+\frac{\partial v}{\partial y}=0\,, \tag{1}$$

$$\frac{\partial u}{\partial t}+u\frac{\partial u}{\partial x}+v\frac{\partial u}{\partial y}=-\frac{1}{\rho}\frac{\partial p}{\partial x}+\vartheta\left(\frac{\partial^2 u}{\partial x^2}+\frac{\partial^2 u}{\partial y^2}\right), \tag{2}$$

$$\frac{\partial v}{\partial t}+u\frac{\partial v}{\partial x}+v\frac{\partial v}{\partial y}=-\frac{1}{\rho}\frac{\partial p}{\partial y}+\vartheta\left(\frac{\partial^2 v}{\partial x^2}+\frac{\partial^2 v}{\partial y^2}\right), \tag{3}$$

where u, v are the velocity components, ρ refers to fluid density, p is pressure, and ϑ refers to the kinematic viscosity. Additionally, for incompressible 2D flows, the above mentioned N-S equations can be simplified in terms of stream function (ψ) and vorticity (ω) as dependent variables. The vorticity (ω) at any point in the plane is expressed as $\omega=\nabla\times\boldsymbol{u}$. Here $\boldsymbol{u}=u\hat{\imath}+v\hat{\jmath}+w\hat{k}$. For x-y plane, $\omega=\omega\times\hat{k}=\left(\partial v/\partial x-\partial u/\partial y\right)$. Moreover, for 2D incompressible fluid flows (x-y plane), we define a scalar function (ψ), which identically satisfies the continuity Eq. (1) as $\boldsymbol{u}=\nabla\times\psi\hat{k}$. This gives us $u=\partial\psi/\partial y$ and $v=-\partial\psi/\partial x$. Now, by differentiating Eqs. (2) and (3) and using the above definitions, the Navier-Stokes equations in the form of a vorticity-streamline function, under steady-state conditions, can be expressed as:

$$\frac{\partial^2\psi}{\partial x^2}+\frac{\partial^2\psi}{\partial y^2}=-\omega, \tag{4}$$

$$\frac{\partial\omega}{\partial t}+u\frac{\partial\omega}{\partial x}+v\frac{\partial\omega}{\partial y}=\frac{1}{\mathrm{Re}}\left(\frac{\partial^2\psi}{\partial x^2}+\frac{\partial^2\psi}{\partial y^2}\right), \tag{5}$$

where $\mathrm{Re}=uy/\vartheta$ is the Reynolds number and (u, v) are the velocity components of the macroscopic velocity.

3 Numerical methodology

3.1 Lattice Boltzmann method with BGK approximation

The present study uses the lattice Boltzmann (LB) technique [25–27] with the D2Q9 model to simulate the flow field behavior. This technique is based on a mesoscopic approach and relies on the theory of the particle distribution function, which numerically solves the equation of kinetic theory for the particle distribution function $f(x, c, t)$, where x denotes the particle's location with lattice velocity c at time t. Generally, the LB equation [15] is solved in two key steps: streaming and collision. In the first step, fluid particles move along the lattice links with specific lattice velocities. Then collision of fluids particles and their redistribution is followed in the second step. The evolution equation for the lattice Boltzmann method is defined as follows in Eq. (6):

$$\frac{\partial f_\alpha}{\partial t}+c_\alpha\times\nabla f_\alpha=\Omega_\alpha\left(f\right), \tag{6}$$

where f_α is the particle distribution function at lattice node x_α with lattice velocity or discrete particle velocity c_α. Ω_α is the collision operator. The collision operator Ω_α can be simplified by Bhatnagar-Gross–Krook (BGK) approximation [23] based on a single relaxation time (SRT) approximation. The accuracy of the LBGK model is of second order in both space and time. The discretized form of Eq. (6) with BGK approximation can be written as:

$$f_\alpha\left(x+c_\alpha\Delta t,t+\Delta t\right)-f_\alpha\left(x,t\right)=\Omega_\alpha\left(f\right), \tag{7}$$

where:

$$\Omega_\alpha\left(f\right)=-\frac{f_\alpha\left(x,t\right)-f_\alpha^{eq}\left(x,t\right)}{\tau},$$

where τ is referred as the relaxation time and $f_\alpha^{eq}\left(x,t\right)$ as the equilibrium distribution function.

3.2 Two-dimensional nine velocity (D2Q9) square lattice model

As shown in Fig. 3, the D2Q9 model uses a square lattice in which each node point has eight neighbors connected by eight lattice links. The fluid particles stream via these lattice links to neighbor nodes with given lattice velocity or discrete particle velocities. The zero location in the above figure refers to the zero lattice velocity, which means the fluid particle does not move anywhere inside the lattice. Moreover, the discrete particle velocities for the D2Q9 square lattice model are defined as follows in Eq. (8):

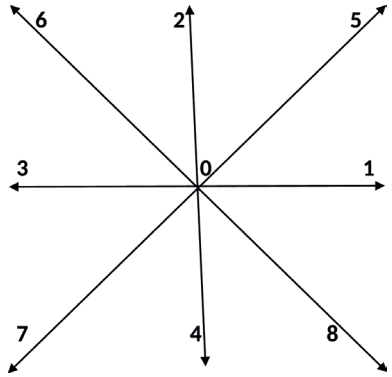

Fig. 3 Two-dimensional nine-velocity (D2Q9) model for lattice Boltzmann method

$$c_\alpha = \begin{cases} 0, & \alpha = 0 \\ c\begin{pmatrix} \cos\left[\dfrac{(\alpha-1)\pi}{2}\right], \\ \sin\left[\dfrac{(\alpha-1)\pi}{2}\right] \end{pmatrix} & \alpha = 1,2,3,4, \\ \sqrt{2}c\begin{pmatrix} \cos\left[\dfrac{(2\alpha-1)\pi}{4}\right], \\ \sin\left[\dfrac{(2\alpha-1)\pi}{4}\right] \end{pmatrix} & \alpha = 5,6,7,8 \end{cases} \tag{8}$$

where $c = \Delta x/\Delta t$ is the lattice speed.

The recovery of the Navier Stokes equation for the LB equation can be ascertained by following these two relations between macroscopic and microscopic states, obtained by Chen at al. [20].

$$\rho = \sum_{\alpha=0}^{8} f_\alpha \tag{9}$$

$$\rho \boldsymbol{u} = \sum_{\alpha=0}^{8} f_\alpha c_\alpha \tag{10}$$

The pressure can be directly calculated from here using $P = \rho c_s^2$, where $c_s = 1/\sqrt{3}$ is the speed of sound. Further, the equilibrium distribution function, given by Maxwell-Boltzmann, which is expressed as Qian et al. [24]:

$$f_\alpha^{eq} = \rho w_\alpha \left[1 + \frac{2(c_\alpha \times \boldsymbol{u}) - \boldsymbol{u} \times \boldsymbol{u}}{2c_s^2} + \frac{(c_\alpha \times \boldsymbol{u})^2}{2c_s^4}\right], \tag{11}$$

where w_α denotes the weights for the D2Q9 model.

$$w_\alpha = \begin{cases} \dfrac{4}{9}, & \alpha = 0, \\ \dfrac{1}{9}, & \alpha = 1,2,3,4 \\ \dfrac{1}{36}, & \alpha = 5,6,7,8 \end{cases} \tag{12}$$

Using the Chapman-Enskog analysis [14], the kinematic viscosity of the fluid can be related to the relaxation factor as:

$$\nu = \frac{\Delta x^2 c_s^2}{\Delta t}\left(\tau - \frac{1}{2}\right). \tag{13}$$

3.3 Boundary conditions

The need for the boundary conditions in the numerical simulations of any physical fluid dynamics phenomena is as essential as the need for carbon dioxide in the trees. As there are many sources of carbon dioxide for the trees, there are several types of boundary conditions for the LBM in the same manner. In the present study bounce-back scheme is employed on the stationary and non-stationary walls [16]. In this scheme, when a fluid particle hits the stationary wall, it streams back in the opposite direction, and when it hits the moving wall, it streams back carrying a small amount of momentum. For a stationary bottom wall of the cavity, it is defined as:

$$f_{2,n} = f_{4,n-1},\ f_{5,n} = f_{7,n-1},\ f_{6,n} = f_{8,n-1}.$$

3.4 Skin friction coefficient and kinetic energy density function

The non-dimensional form of skin friction coefficient for moving horizontal and vertical walls is calculated as:

$$\left(C_f\right)_H = \frac{2}{\mathrm{Re}}\left(\frac{dU}{dY}\right)_H,$$

$$\left(C_f\right)_V = \frac{2}{\mathrm{Re}}\left(\frac{dV}{dX}\right)_V,$$

respectively. Here U and V are the non-dimensional horizontal and vertical components of velocity, respectively. Subscripts H and V denote to the skin friction coefficient on the horizontal and vertical solid walls, respectively. Furthermore, the kinetic energy density function for inserted fluid inside the cavity is calculated as:

$$E = \frac{1}{2}\sum_{i,j}\left(U^2 + V^2\right).$$

4 Numerical experiments

4.1 Grid independence test

To select an optimum grid for the numerical simulations of the present phenomenon, the authors have carried out a study of horizontal velocity profile and vertical velocity profile with vertical centerline and horizontal centerline, respectively, for a one-sided lid-driven cavity for four different types of grids 51 × 51, 101 × 101, 151 × 151, 201 × 201. The obtained results are displayed in Fig. 4. It is highlighted from Fig. 4 that both the velocity profiles obtained with grids 101 × 101, 151 × 151, and 201 × 201 are almost identical, whereas the velocity profiles obtained with grid size 51 × 51 are slightly deviated at some places compared to the other three higher-order grids. Hence, in view of computational cost, a grid size 101 × 101 is selected for all further simulations.

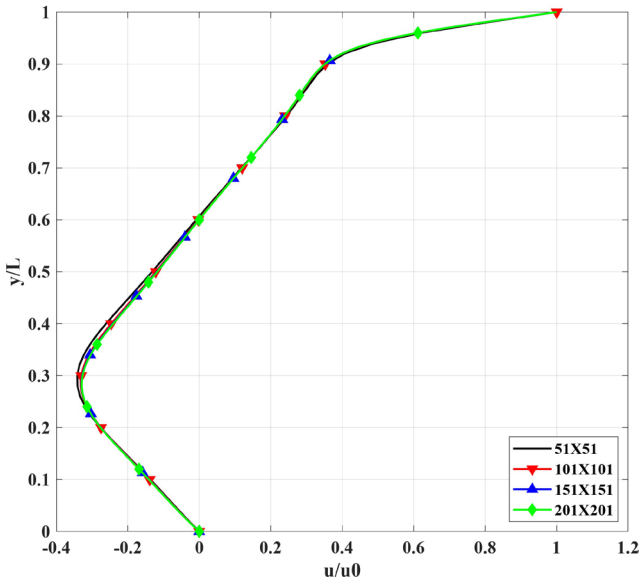

(a)

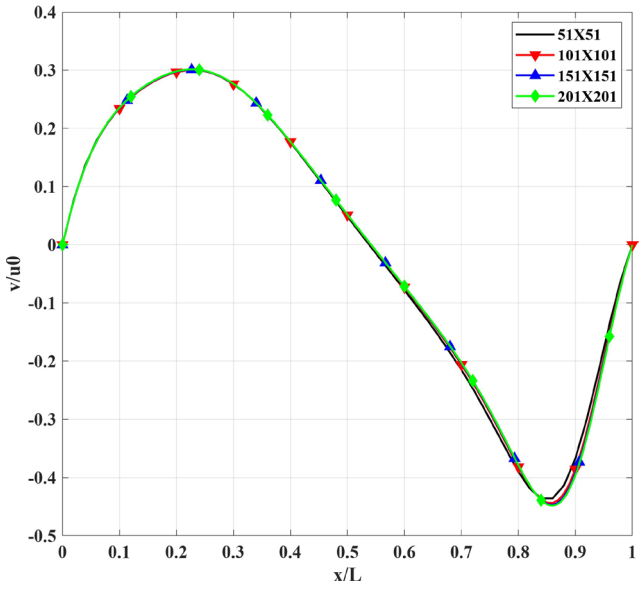

(b)

Fig. 4 Grid independence test for; (a) Horizontal velocity at vertical centerline for Re = 400 at various grid sizes; (b) Vertical velocity at horizontal centerline for Re = 400 at various grid sizes

4.2 Validation of the code

To verify the present methodology, a comparison of the horizontal and vertical velocity profiles have been carried out with the existing literature by Ghia et al. [28] for a one-sided lid-driven square cavity (Fig. 5). The Reynolds number and the grid size are chosen to be 400 and 101 × 101 for the comparison. One can conclude that the results obtained with the present methodology are in remarkable agreement with the existing ones, which shows the present methodology's accuracy.

5 Results and discussion

Numerical simulations are carried out to examine the behavior of fluid flow formed by two adjacent-sided lid-driven square cavities. Inside the cavity, the inserted fluid has kinematic viscosity and density around 10^{-6} m^2/sec and 1000 kg/m^3 at 20 °C respectively, but when we introduce matching principle between the physical domain and the lattice domain [15], the lattice kinematic viscosity calculates to be 0.01. The Reynolds number is varied for a wide range starting from 100. All the results are simulated up to an accuracy of 10^{-8} using the following relative error condition:

$$\left|\frac{q^{n+1}(i,j)-q^{n}(i,j)}{q^{n+1}(i,j)}\right|<10^{-8},$$

where $q^n(i,j)$ denotes the net velocity of the fluid particle at (i,j) coordinate and at the time step $t^n = n\Delta t$.

5.1 Two adjacent-sided diverging lid-driven square cavity

The geometry of the two-adjacent-sided lid-driven square cavity is shown in Fig. 1. The fluid flow is driven by the top wall being moved rightwards and the left wall being moved downwards simultaneously with identical speeds. The streamlines for various Reynolds numbers for the present phenomena are plotted in Fig. 6. It is noted that streamlines for Re = 100, 400, and 1000 are found to be symmetric with respect to one of the diagonals of the cavity, and this

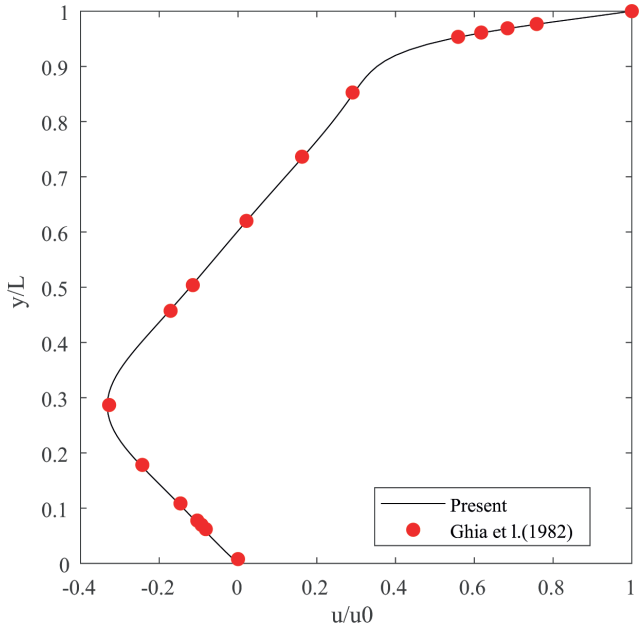

(a)

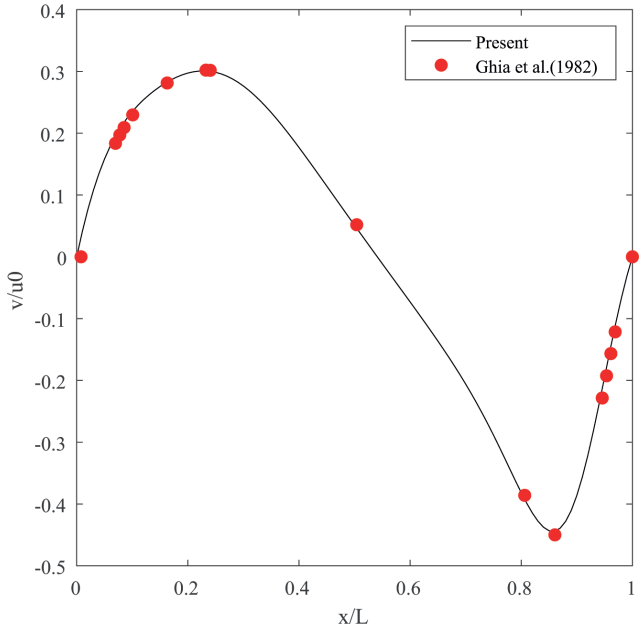

(b)

Fig. 5 Velocity profiles for code validation at the grid size 101 × 101 for Re = 400; (a) Horizontal u-velocity; (b) Vertical v-velocity

symmetry is preserved up to a maximum Reynolds number of 1120 (Fig. 6 (d)). At a critical Reynolds number of Re = 1121 (Fig. 6 (e)), the streamlines start to tend to obtain an asymmetric form, and this asymmetry in flow develops continuously further with the increment of the Reynolds number (Fig. 6 (f)–(i)). At Re = 2500, the asymmetry becomes so high that among the two primarily counter-rotating vortices, one primarily vortex dominates the flow region (Fig. 6 (j)), whereas, in the case of a low Reynolds number (near Re = 1120), such phenomenon is lesser.

There are two reasons behind the development of this asymmetry:

1. The turbulence flow starts to develop with the increase of Re;
2. The inertia effect, due to the motion of fluid particles, is increased to a great extent dominating over viscous nature of fluid at the higher Reynolds number.

Re = 1121 is such a critical Reynolds number where the flow starts to take asymmetric form because of these two reasons. Moreover, at Re = 100 (Fig. 6 (a)), only two primarily counter-rotating vortices appear, whereas, for Re = 400 or higher (Fig. 6 (b) and (c)), two secondary vortices can also be seen developing at the right bottom of the cavity. It is informed that a dark diagonal black line in the streamline plots up to Re = 1121 is manually drawn. That line should not be considered a streamline because that line is drawn to represent only symmetry.

We know that due to the existence of large velocity gradients near the solid moving walls, the frictional force gets generated. In fluid dynamics, this frictional force is expressed in terms of skin friction coefficient. Table 1 represents the distribution of total skin friction coefficient for horizontal top wall and vertical left wall. Initially, we note that the total skin friction coefficient at the top and left wall are identical and it remains identical until the symmetry of streamlines breaks down. At Re = 1121, the two values of total C_f start to alter, and the primary vortex starts to dominate inside the cavity resulting in a shrink of another vortex at the left wall, which induces the large velocity gradients near the left wall.

Hence an increased frictional force can be observed from Table 1 above Re = 1121 near the left wall. Table 1 also shows the distribution of the total kinetic energy density function, which can be used as verification of mathematical models. In the present study, the Reynolds number is increased by increasing the lid velocities and keeping viscosity constant. Therefore, whenever Reynolds number is increased, fluid particles start to accelerate inside the cavity, and this acceleration of particles boosts the overall kinetic energy, which can be illuminated from Table 1.

Fig. 7 displays the convergence rate of the present methodology for various Reynolds numbers for the present phenomena. Note that this convergence rate is not displayed for all those Reynolds numbers which were chosen above

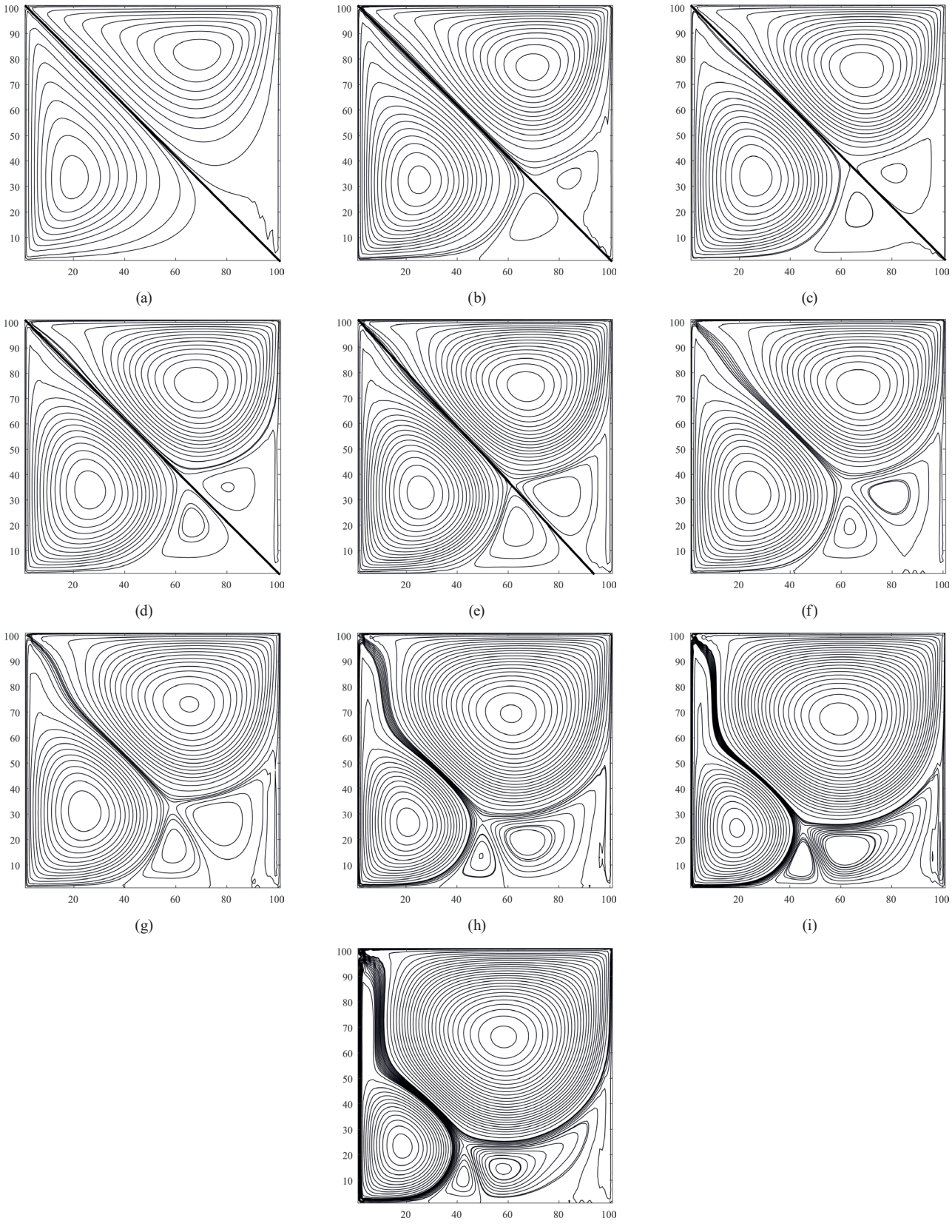

Fig. 6 Streamlines of fluid flow inside the two adjacent-sided diverging lid-driven square cavity at various Reynolds numbers; (a) Re = 100; (b) Re = 400; (c) Re = 1000; (d) Re = 1120; (e) Re = 1121; (f) Re = 1125; (g) Re = 1200; (h) Re = 1500; (i) Re = 2000; (j) Re = 2500

Table 1 Skin friction coefficient on left and top wall, and total kinetic energy distributions against the Reynolds numbers for diverging driven cavity

Re	$(C_f)_H$	$(C_f)_V$	Kinetic energy distribution (E)
100	0.4748	0.4748	0.0577
400	0.5420	0.5420	1.0033
1000	0.6252	0.6252	6.8260
1121	0.6328	0.6421	8.6716
1125	0.6330	0.6432	8.7366
1200	0.6340	0.6581	10.0056
1500	0.6485	0.7071	15.9565
2000	0.6786	0.7576	29.2307
2500	0.7006	0.8000	46.9756

to obtain flow behavior that is due to the overlapping of the graphs of some Reynolds numbers, but that should not be an issue because a well accurate convergence rate be shown in the Fig. 7 (a).

The results are displayed on a logarithmic scale for both the axes, and the plotting is carried out between the required number of time steps and the desired accuracy. The higher the number of time steps required to achieve the desired accuracy refers to the lesser methodology's convergence rate. It is concluded that the number of time steps required to achieve the desired accuracy for Re = 100 is minimum. In other words, the convergence rate of Re = 100 is maximum, and with the increase of the Reynolds number, the convergence rate starts to reduce, and at the critical Reynolds number, it becomes minimum (Fig. 7 (b)).

But, after surpassing the critical Reynolds number, the converse process starts to take place, i.e., now, with the increment of the Reynolds number, the convergence rate also starts to increase, and for the Re = 2000, the convergence rate eventually becomes almost equal to the convergence rate of Re = 1000.

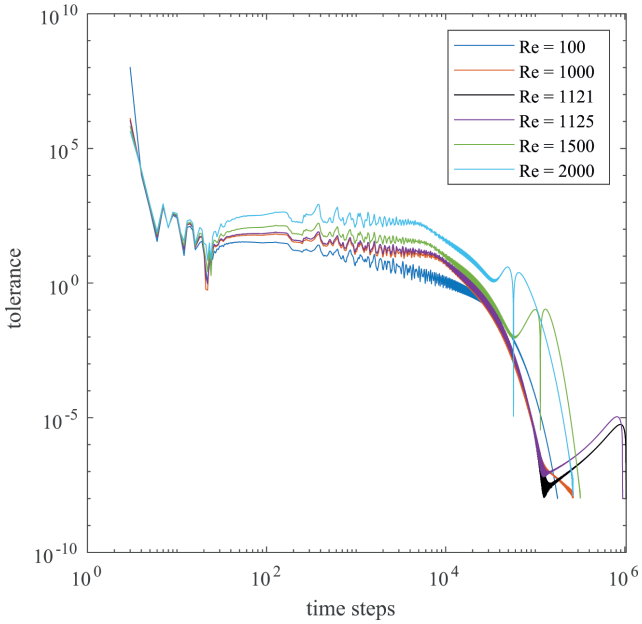

(a)

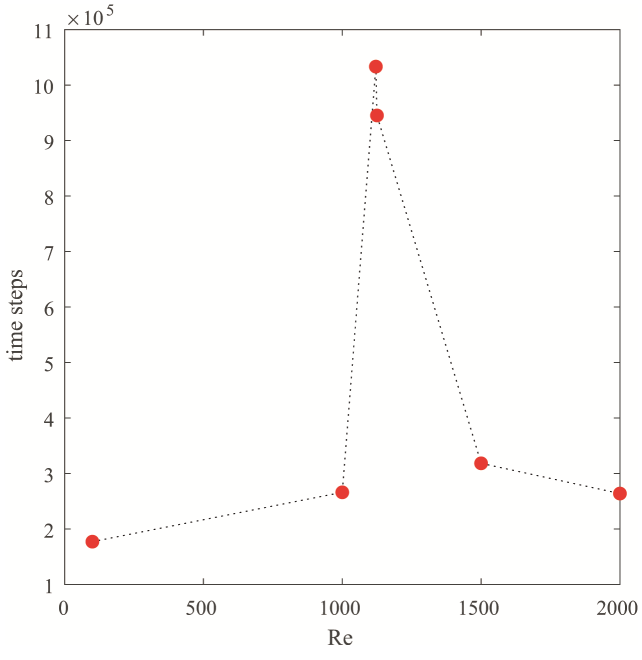

(b)

Fig. 7 Convergence rate of the lattice Boltzmann method; (a) relative error vs. time; (b) time steps vs. Reynolds number

5.2 Two adjacent-sided converging lid-driven square cavity

The geometry of the two-adjacent-sided converging lid-driven square cavity is shown in Fig. 2. The fluid flow is driven by the top wall being moved rightwards and the right wall being moved upwards simultaneously with identical speeds so that they seem to converge at point B of the cavity. The streamlines for various Reynolds numbers, starting from 100, are displayed in Fig. 8 with some surprising results this time as the symmetry of the streamlines breaks two times. For low Reynolds numbers, the streamlines were found to be symmetric with respect to another diagonal of the cavity (Fig. 8 (a) and (b)), and this symmetry in flow preserves itself up to Re = 968 (Fig. 8 (c)).

The Re = 969 is the first critical Reynolds number where the asymmetry state starts to occur (Fig. 8 (d)). Above this first critical Reynolds number, the asymmetry develops continuously more and more inside the cavity, and at Re = 1199, this first asymmetric state ends (Fig. 8 (e)). After surpassing this range of Reynolds numbers

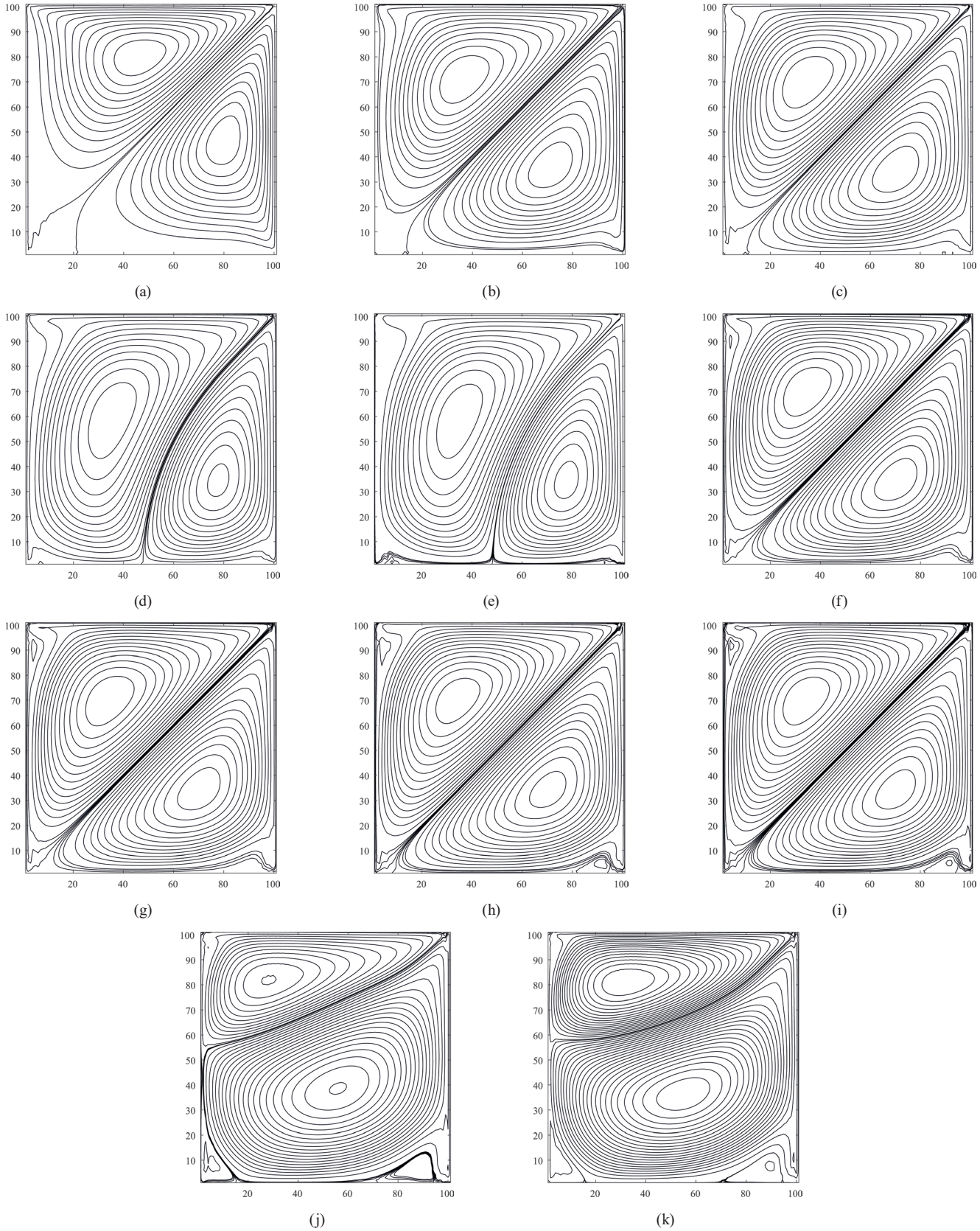

Fig. 8 Streamlines of fluid flow inside the two adjacent-sided converging lid-driven square cavity; (a) Re = 100; (b) Re = 400; (c) Re = 968; (d) Re = 969; (e) Re = 1199; (f) Re = 1200; (g) Re = 1500; (h) Re = 2000; (i) Re = 2052; (j) Re = 2053; (k) Re = 2100

(Re = 969–1199), the flow behavior stabilizes itself and streamlines occupy symmetric form with respect to the same diagonal along with a secondary vortex at the top left corner of the cavity(Fig. 8 (f)) and then this time, with the increment of Reynolds number, symmetry of streamlines preserves itself up to Re = 2052 with two secondary vortices (Fig. 8 (g)–(i)).

The second critical Reynolds number is found to be 2053, where streamlines again lose their symmetry (Fig. 8 (j)), and the second asymmetric state comes into account. Moreover, the asymmetry obtained in the streamlines for the second critical Reynolds number defers from the asymmetry obtained in the streamlines for the first critical Reynolds number. This difference can be understood as the streamlines for the first critical Reynolds number divert to the right side of the cavity, whereas in the second case, they divert to the top side of the cavity.

Note that the simulations for this case are carried out up to Re = 2100. That is because this methodology starts to provide unstable solutions for this case at higher Reynolds numbers. However, the streamlines obtained up to Re = 2100 have already proved the importance of the present methodology (Fig. 8 (k)).

Table 2 represents the total skin friction coefficient distribution at the horizontal top wall and vertical right wall for converging driven cavity. We again note that, up to the formation of symmetry of streamlines (Re = 968), the total skin friction coefficient at the top and right walls remains identical. During the first asymmetric state (Re = 969–1199), we see that dominating vortex is the vortex generated by the top wall, and this dominating vortex shrinks the vortex generated by the right wall. Hence, it is expected that, due to the existence of large velocity gradients at the right wall, C_f at the vertical right wall must increase. However, Table 2 shows that the C_f at vertical right wall decreases for the first asymmetric state. This occurs because, in the present study, the vertical wall is considered to be positive in the vertical downward direction and negative in the vertical upward direction (Figs. 1 and 2). The same phenomena can be illuminated for the second critical stage from Table 2. The total kinetic energy of fluid particles was again observed to be as expected (increasing with the increase of Reynolds number).

The rate of convergence of the present methodology for this case is the same as the previous one, the critical Reynolds numbers take much time to reach the given accuracy, whereas the Reynolds numbers, which provide a symmetric form of streamlines, reach the given accuracy in a less time.

Table 2 Skin friction coefficient on left and top wall, and total kinetic energy distributions against the Reynolds number for converging driven cavity

Re	$(C_f)_H$	$(C_f)_V$	Kinetic energy distribution (E)
100	0.4741	0.4741	0.0687
400	0.5559	0.5559	1.4693
800	0.6395	0.6395	6.4445
900	0.6568	0.6568	8.2516
950	0.6650	0.6650	9.2386
968	0.6679	0.6679	9.5075
969	0.7027	0.6131	9.5559
1000	0.7084	0.6164	10.2086
1199	0.7437	0.6348	14.8890
1200	0.7027	0.7027	14.9939
1500	0.7410	0.7410	23.6425
2000	0.8960	0.7960	41.9717
2052	0.8015	0.8015	44.1322
2053	0.7121	0.8529	46.9626
2100	0.6572	0.8810	48.5440

6 Conclusion

The present study explores the configurations of numerical simulations for a two adjacent-sided converging and diverging lid-driven square cavity. The simulation results are performed by the lattice Boltzmann method with an SRT scheme using the D2Q9 model. The LBM code used in the study is validated by comparison with existing benchmark results.

The following conclusions have been drawn in the present study:

- In two adjacent-sided diverging lid-driven square cavity, besides two primary vortices, a pair of counter-rotating secondary vortices form for above Re = 100, and only one critical Reynolds number (Re = 1153) is observed, which differs the symmetric and asymmetric state of the streamlines;
- Two critical Reynolds numbers are recorded in two adjacent-sided converging lid-driven square cavity, resulting in two asymmetric states of streamlines;
- The streamlines, in the converging case, were found to be diverting in opposite directions for the two asymmetric states, and the secondary vortices started to form after surpassing the first asymmetric state (Re = 1200);
- The distribution of total kinetic energy is independent of the formation of streamlines and critical stages as expected, it always increases with the increase of the Reynolds number;
- The smaller primary vortex imposed wall has a higher value of skin friction coefficient than the

one large primary vortex imposed wall if velocity is chosen to be positive;

- The rate of convergence was recorded to be least for the critical Reynolds numbers.

Acknowledgement

This work was supported to Mahendra Yadav by the CSIR-HRDG Ph.D. grant (09/149(0787) /2019-EMR-I), Ministry of Science \& Technology, Government of India.

References

[1] Aidun, C. K., Triantafillopoulos, N. G., Benson, J. D. "Global stability of a lid-driven cavity with throughflow: Flow visualization studies", Physics of Fluids A: Fluid Dynamics, 3(9), pp. 2081–2091, 1991. https://doi.org/10.1063/1.857891

[2] Shankar, P. N., Deshpande, M. D. "Fluid Mechanics in the Driven Cavity", Annual Review of Fluid Mechanics, 32(1), pp. 93–136, 2000. https://doi.org/10.1146/annurev.fluid.32.1.93

[3] Wahba, E. M. "Multiplicity of states for two-sided and four-sided lid driven cavity flows", Computers & Fluids, 38(2), pp. 247–253, 2009. https://doi.org/10.1016/j.compfluid.2008.02.001

[4] Mendu, S. S., Das, P. K. "Fluid flow in a cavity driven by an oscillating lid—A simulation by lattice Boltzmann method", European Journal of Mechanics - B/Fluids, 39, pp. 59–70, 2013. https://doi.org/10.1016/j.euromechflu.2012.12.002

[5] Biswas, S., Kalita, J. C. "Topology of corner vortices in the lid-driven cavity flow: 2D vis a vis 3D", Archive of Applied Mechanics, 90(10), pp. 2201–2216, 2020. https://doi.org/10.1007/s00419-020-01716-0

[6] Dalai, B., Laha, M. K. "Numerical Solution of Steady Incompressible Flow in a Lid-Driven Cavity Using Alternating Direction Implicit Method", In: Singh, B. N., Roy, A., Maiti, D. K. (eds.) Recent Advances in Theoretical, Applied, Computational and Experimental Mechanics, Springer, 2020, pp. 353–364. ISBN 978-981-15-1188-2 https://doi.org/10.1007/978-981-15-1189-9_28

[7] Sikdar, P., Dash, S. M., Sinhamahapatra, K. P. "Lattice Boltzmann simulations of a lid-driven cavity at different moving lengths of the top lid", In: Prabu, T., Viswanathan, P., Agrawal, A., Banerjee, J. (eds.) Fluid Mechanics and Fluid Power, Springer, 2021, pp. 203–211. ISBN 978-981-16-0697-7 https://doi.org/10.1007/978-981-16-0698-4_22

[8] Abedini, A., Ivaz, K., Shahmorad, S., Dadvand, A. "Numerical solution of the time-fractional Navier–Stokes equations for incompressible flow in a lid-driven cavity", Computational and Applied Mathematics, 40(1), 34, 2021. https://doi.org/10.1007/s40314-021-01413-w

[9] Álvarez Hostos, Salazar Bove, J. C., Cruchaga M. A., Fachinotti, V. D., Mujica Agelvis, R. A. "Solving steady-state lid-driven square cavity flows at high Reynolds numbers via a coupled improved element-free Galerkin–reduced integration penalty method", Computers & Mathematics with Applications, 99, pp. 211–228, 2021. https://doi.org/10.1016/j.camwa.2021.08.013

[10] Azzouz, E. A., Houat, S. "Numerical Solutions of Steady Flow in a Three-Sided Lid-Driven Square Cavity", International Journal of Applied and Computational Mathematics, 8(3), 118, 2022. https://doi.org/10.1007/s40819-022-01314-4

[11] Patel, M. R., Pandya, J. U., Patel, V. K. "Numerical Analysis of Fluid Flow Behaviour in Four-Sided Square Lid-Driven Cavity Using the Finite Volume Technique", International Journal of Applied and Computational Mathematics, 8(4), 153, 2022. https://doi.org/10.1007/s40819-022-01353-x

[12] Turkyilmazoglu, M. "Driven flow motion by a dually moving lid of a square cavity", European Journal of Mechanics - B/Fluids, 94, pp. 17–28, 2022. https://doi.org/10.1016/j.euromechflu.2022.02.005

[13] Zhang, K., Jing, H.-F., Feng, X.-F., Jiang, Y.-L. "Numerical investigation of flow structures in multi-sided lid-driven cubic cavities with various ratios by MRT-LBE", Chinese Journal of Physics, 77, pp. 2472–2489, 2022. https://doi.org/10.1016/j.cjph.2022.03.044

[14] Succi, S. "The Lattice Boltzmann Equation for Fluid Dynamics and Beyond", Oxford University Press, 2001. ISBN 9780198503989 https://doi.org/10.1093/oso/9780198503989.001.0001

[15] Mohamad, A. A. "Lattice Boltzmann Method: Fundamentals and Engineering Applications with Computer Codes", Springer, 2011. ISBN 978-1-4471-6099-1 https://doi.org/10.1007/978-0-85729-455-5

[16] Krüger, T., Kusumaatmaja, H., Kuzmin, A., Shardt, O., Silva, G., Viggen, E. M. "The Lattice Boltzmann Method: Principles and Practice", Springer, 2016. ISBN 978-3-319-44647-9 https://doi.org/10.1007/978-3-319-44649-3

[17] Hardy, J., Pomeau, Y., de Pazzis, O. "Time evolution of a two-dimensional model system. I. Invariant states and time correlation functions", Journal of Mathematical Physics, 14(12), pp. 1746–1759, 1973. https://doi.org/10.1063/1.1666248

[18] Hardy, J., de Pazzis, O., Pomeau, Y. "Molecular dynamics of a classical lattice gas: Transport properties and time correlation functions", Physical Review A, 13(5), pp. 1949–1961, 1976. https://doi.org/10.1103/PhysRevA.13.1949

[19] Frisch, U., Hasslacher, B., Pomeau, Y. "Lattice-Gas Automata for the Navier-Stokes Equation", Physical Review Letters, 56(14), pp. 1505–1508, 1986. https://doi.org/10.1103/PhysRevLett.56.1505

[20] Chen, H., Chen, S., Matthaeus, W. H. "Recovery of the Navier-Stokes equations using a lattice-gas Boltzmann method", Physical Review A, 45(8), pp. R5339–R5342, 1992. https://doi.org/10.1103/PhysRevA.45.R5339

[21] He, X., Luo, L.-S. "A priori derivation of the lattice Boltzmann equation", Physical Review E, 55(6), pp. R6333–R6336, 1997. https://doi.org/10.1103/PhysRevE.55.R6333

[22] He, X., Luo, L.-S. "Theory of the lattice Boltzmann method: From the Boltzmann equation to the lattice Boltzmann equation", Physical Review E, 56(6), pp. 6811–6817, 1997. https://doi.org/10.1103/PhysRevE.56.6811

[23] Bhatnagar, P. L., Gross, E. P., Krook, M. "A Model for Collision Processes in Gases. I. Small Amplitude Processes in Charged and Neutral One-Component Systems", Physical Review, 94(3), pp. 511–525, 1954. https://doi.org/10.1103/PhysRev.94.511

[24] Qian, Y. H., D'Humières, D., Lallemand, P. "Lattice BGK Models for Navier-Stokes Equation", Europhysics Letters, 17(6), pp. 479–484, 1992. https://doi.org/10.1209/0295-5075/17/6/001

[25] An, B., Bergadà, J. M., Sang, W. M. "A simplified new multigrid algorithm of lattice Boltzmann method for steady states", Computers & Mathematics with Applications, 135, pp. 102–110, 2023. https://doi.org/10.1016/j.camwa.2023.01.013

[26] Wen, M., Wang, Y., Li, W., Zhao Z. "An improved gas kinetic BGK scheme for finite volume lattice Boltzmann method for nearly incompressible flows", Computers & Fluids, 255, 105822, 2023. https://doi.org/10.1016/j.compfluid.2023.105822

[27] Ni, A. É. "Hybrid Method of Lattice Boltzmann Equations to Model Thermogravitational Flows", Journal of Engineering Physics and Thermophysics, 94(2), pp. 415–422, 2021. https://doi.org/10.1007/s10F891-021-02326-5

[28] Ghia, U., Ghia, K. N., Shin, C. T. "High-Re solutions for incompressible flow using the Navier-Stokes equations and a multigrid method", Journal of Computational Physics, 48(3), pp. 387–411, 1982. https://doi.org/10.1016/0021-9991(82)90058-4